A Nature Portfolio journal



https://doi.org/10.1038/s43856-025-01055-7

# Predictive computational framework to provide a digital twin for personalized cardiovascular medicine

Check for updates

Mengzhe Lyu ® <sup>1,2</sup> ⋈, Ryo Torii ® <sup>1</sup> ⋈, Ce Liang ® <sup>1</sup>, Xuehuan Zhang <sup>3</sup>, Xifu Wang <sup>4</sup>, Qiaoqiao Li <sup>5</sup>, Yiannis Ventikos <sup>3,6</sup> & Duanduan Chen ® <sup>3</sup> ⋈

#### **Abstract**

**Background** In percutaneous coronary intervention (PCI), the ability to predict post-PCI fractional flow reserve (FFR) and stented vessel informs procedural planning. However, highly precise and effective methods to quantitatively simulate coronary intervention are lacking. This study developed and validated a virtual coronary intervention (VCI) technique for non-invasive physiological and anatomical assessment of PCI.

**Methods** In this study, patients with substantial lesions (pre-PCI CT-FFR of less than 0.80) were enrolled. VCI framework was used to predict vessel reshape and post-PCI CT-FFR. The accuracy of predicted post-VCI CT-FFR, luminal cross-sectional area (CSA) and centreline curvature was validated with post-PCI computed tomography (CT) angiography datasets.

**Results** Overall, 30 patients are initially screened; 21 meet the inclusion criteria, and 9 patients (9 vessels) are included in the final analysis. The average PCI-simulation time is  $24.92 \pm 1.00 \, \text{s}$  on a single processor. The calculated post-PCI CT-FFR is  $0.92 \pm 0.09$ , whereas the predicted post-VCI CT-FFR is  $0.90 \pm 0.08$  (mean difference:  $-0.02 \pm 0.05$  FFR units; limits of agreement: -0.08 to 0.05). Morphologically, the predicted CSA is  $16.36 \pm 4.41 \, \text{mm}^2$  and the post-CSA is  $17.91 \pm 4.84 \, \text{mm}^2$  (mean difference:  $-1.55 \pm 1.89 \, \text{mm}^2$ ; limits of agreement:  $-5.22 \, \text{to} \, 2.12$ ). The predicted centreline curvature across the stented segment (including  $\sim 2 \, \text{mm}$  proximal and distal margins) is

**Conclusions** The proposed VCI technique achieves non-invasive pre-procedural anatomical and physiological assessment of coronary intervention. The proposed model has the potential to optimize PCI pre-procedural planning and improve the safety and efficiency of PCI.

 $0.15 \pm 0.04$  mm<sup>-1</sup>, while the post-PCI centreline curvature is  $0.17 \pm 0.03$  mm<sup>-1</sup> (mean

#### **Plain Language Summary**

This study aimed to help doctors plan heart procedures more accurately. A common treatment is insertion of a stent, which is a small, mesh-like tube that is inserted into a blood vessel to keep it open. A computer simulation tool that can predict how a patient's heart artery will look and function after a stent is placed was developed. It was tested using scan data from patients and found that it could closely match real posttreatment results. The tool was fast, taking under 30 s to run, and was able to model both blood flow and artery shape. These findings suggest that this method could improve how doctors plan treatments for blocked heart arteries, making procedures safer and more effective. In the future, it may help personalize care and reduce unnecessary risks during heart interventions.

The observation of fractional flow reserve (FFR) instantly after stent deployment can be used to evaluate functional revascularization gained from percutaneous coronary intervention (PCI)<sup>1</sup>. A better prognosis has been demonstrated for patients with high FFR readings following PCI than for those with low post-PCI FFR<sup>2-4</sup>. Patients with a post-treatment FFR of less than 0.90 may be more likely to develop major adverse cardiac events

difference:  $-0.02 \pm 0.06$  mm<sup>-1</sup>; limits of agreement: -0.12 to 0.09).

(MACE) at follow-up, and a higher post-PCI FFR is related to better PCI outcome<sup>5-7</sup>. It has been previously observed that after PCI, approximately one-third of patients who still have inadequate FFR and angina persists for 20% to 50% of patients<sup>8</sup>. Additionally, complications of PCI may affect patient survival and healthcare costs<sup>9-11</sup>. There is a positive correlation between patient risk and the procedural complexity of PCI. It is crucial to be

<sup>1</sup>Department of Mechanical Engineering, University College London, London, UK. <sup>2</sup>Siemens Healthineers Digital Technology (Shanghai) Co. Ltd., Shanghai, China. <sup>3</sup>School of Medical Technology, Beijing Institute of Technology, Beijing, China. <sup>4</sup>Department of Emergency and Critical Care Center, Beijing Anzhen Hospital Affiliated to Capital Medical University, Beijing, China. <sup>5</sup>School of International Education, University of International Business and Economics, Beijing, China. <sup>6</sup>Faculty of Engineering, Monash University, Clayton, Australia. —e-mail: ucemmly@ucl.ac.uk; r.torii@ucl.ac.uk; duanduan@bit.edu.cn

aware of the potential complications of PCI, such as hemodynamic collapse, entrapped equipment, dissections, etc. <sup>12</sup>. As a result, the development of intracoronary physiological and accurate stent deployment assessment tools that help to determine functional revascularization and vessel remodelling have the potential to improve the efficiency and safety of PCI treatment.

Coronary computed tomography (CT) angiography-based fractional flow reserve (CT-FFR) is a non-invasive physiologic simulation technique that models blood flow based on computed tomography angiogram (CTA) images. As for coronary stenting, research studies on computational patientspecific coronary stenting have received a significant investment recently 13. The finite element (FE) method is typically used in coronary structural investigations and coronary artery bifurcation stenting<sup>13-15</sup>. Prior studies have made substantial contributions to PCI treatment planning, but they are limited in offering clinical practice assistance in real time. Advanced computational techniques that are able to accurately mimic the morphological and hemodynamic changes in the coronary artery caused by the stent in real time are required. One of the solutions is to use virtual coronary intervention (VCI) tools, which aim to give time-efficient simulations for treatment plans<sup>16</sup>. Pioneered by Heartflow Inc., Redwood City, California, CT-FFR Planner is, as far as we are aware, among the first tools capable of accurately predicting post-PCI FFR<sup>1</sup>. Based on the angiogram, Gosling et al.<sup>16</sup> developed a treatment planning tool which can accurately predict virtual (vFFR) with a reasonable computational time. While these studies make significant contributions to PCI planning, the virtual stenting process is implemented by employing a cubic spline to adjust the cross-sectional radius. This adjustment aims to smooth the vessel trajectory based on the dimensions (diameter and length) of the stent. Consequently, the vessel undergoes modifications, and post-PCI CT-FFR is calculated based on the newly created vessel model. There are some limitations in the existing fast coronary virtual stenting method, as there are not physical-oriented models and the balloon is not included in the simulation process. The balloon is frequently used as a pre-dilation, and post-dilation device during the PCI process and it is used to expand the stent. Besides, vessel-stent interaction can affect the simulation results depending on various situations. To develop a more realistic VCI framework, a balloon should be included, and an efficient contact model should be developed along with the dynamic mesh<sup>17</sup> to accurately simulate the balloon expansion process and balloon-attached coronary reshaping with rapid computation time. Therefore, the overall aim of this study is to develop a fast VCI technique that provides intracoronary post-stenting physiological assessment along with anatomical assessment.

This study shows that the patient-specific VCI framework predicts post-PCI CT-FFR and stent-induced geometric changes with prediction errors confined to clinically acceptable limits, and completes each simulation in about 25 s on a single CPU. While these findings suggest the method could aid non-invasive PCI planning.

#### Methods

This study was approved by the Institutional Review Board of Beijing Anzhen Hospital Affiliated to Capital Medical University (KS2023090). Written informed consent was obtained from all participants prior to their inclusion in the study.

#### Study design

The patients who presented with mild-to-moderate chest pain at the Cardiology Department of Beijing Anzhen Hospital Affiliated to Capital Medical University from January 2021 to March 2021 were included in this study. During the study period, a total of 30 patients who underwent coronary CTA both before and after PCI were initially considered for inclusion in this study. However, upon preliminary review, 5 patients were excluded due to incomplete procedural records—such as missing details on balloon inflation pressure, stent deployment location, or device specifications—parameters essential for accurate VCI modeling. An additional 4 patients were excluded due to the absence of key procedural steps, such as balloon pre-dilation or post-dilation. Therefore, 21 patients remained eligible for further evaluation. Among these, patients with pre-PCI CT-FFR greater

than 0.8 (indicating non-severe stenosis), who experienced failed automated image segmentation, were rejected for post-CT-FFR analysis due to issues primarily related to poor vessel segmentation (such as vessel disconnection). The patient enrollment and exclusion pathway is detailed in Supplemental Fig. 1.

9 patients with substantial lesions determined by pre-PCI CT-FFR of less than 0.80 were considered for further study. The patient characteristics and vessel-specific characteristics are shown in Supplemental Table 1. The virtual balloon and stent expansion processes are integrated with flow analysis to create the VCI framework, a tool that, as far as we are aware, is the first to realistically model the PCI procedure and predict post-PCI CT-FFR while accounting for lumen changes (Fig. 1). This computational method includes 5 steps, aiming to achieve both non-invasive physiological assessment and detailed anatomical assessment for PCI. The VCI framework has the potential to provide risk evaluation for PCI procedures.

### Coronary CTA image acquisition, automated geometry reconstruction and post-processing

CTA datasets before and after PCI were obtained using a dual-source CT scanner (SOMATOM Definition Flash, Siemens, Germany). The images were acquired with an injection of 70-90 ml of contrast and 50 ml of saline chaser; a threshold of 80 HU; rotation speed of 500 ms; collimation of 64; slice thickness of 1.0 mm; pitch of 1.0; voltage of 100 kV; and current of 200-350 mA. CCTA images were processed using the CoronaryDoc software (ShuKun Technology, Beijing), which applies deep learning techniques for vascular segmentation, stenosis detection, and the generation of curved planar reformation (CPR) and volume rendering images. Vascular segmentation was performed using an enhanced three-dimensional (3D) U-Net architecture, incorporating a Bottle-Neck model and a progressive iterative prediction network<sup>18</sup>, as shown in Fig. 2a. Subsequently, a hybrid method combining a 3D segmentation neural network and a onedimensional sequential verification approach was applied to MPR and CPR images to detect stenosis. All reconstructions were carried out by a clinician experienced in interpreting CT images and reviewed by a vascular surgeon.

The balloons were computationally generated within the VCI framework in their crimped state, while the stents were modeled based on manufacturer-provided nominal dimensions to ensure accuracy. These structures are illustrated in Fig. 2b, e. A detailed overview of the virtual fast pre-operative process, including balloon folding, pleating, and stent crimping, is provided in Supplemental Fig. 2.

#### **VCI** technique

Theoretical framework. The VCI technique based on the dynamic mesh is used to model the vessel-stent and stent-vessel interactions. The concept of the dynamic mesh, first introduced in the 1990s<sup>19</sup>, is considered the earliest and most classic physical model to have been proposed and applied. In the VCI technique, the models are discretized into particle systems that are linked with fictitious mass, damping, and stiffness elements<sup>20</sup>. The force acting on the spring element obeys Hooke's law. The movement of this dynamic mesh obeys the motion equation of dynamic equilibrium, as shown in the equation below:

$$F_{int} + F_{ext} = ma \tag{1}$$

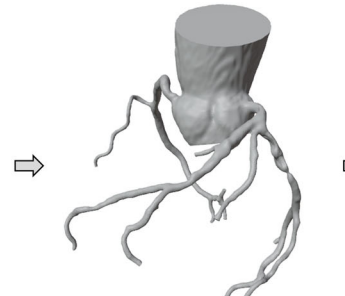
where  $F_{\rm int}$  is the internal force and  $F_{\rm ext}$  is the external force, m is the mass of each vertex  $V_i$ , a is the acceleration caused by forces  $F_{\rm int}$  and  $F_{\rm ext}$ . The internal force is the resultant force caused by spring and damper. The external force corresponds to the contact force of different models, the internal pressure of the balloon and damping force ( $F_{Damping} = -Dv$ ), where D is the system damping coefficient and it is set to 0.9. Such a damping force and damping coefficient (0.9) are frequently used in virtual stenting applications (such as in the work by<sup>21,22</sup>).

The Euler method can be applied to compute the force applied to the vertex  $V_i$  at any given time t. The fundamental equation of dynamics can

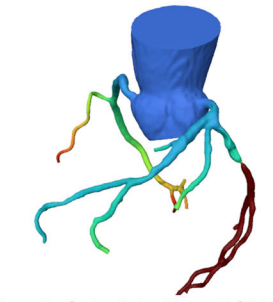


Step 1: CCTA based 3D coronary rendering and model segmentation

Risk evaluation Clinical decision making **Training & Education** 



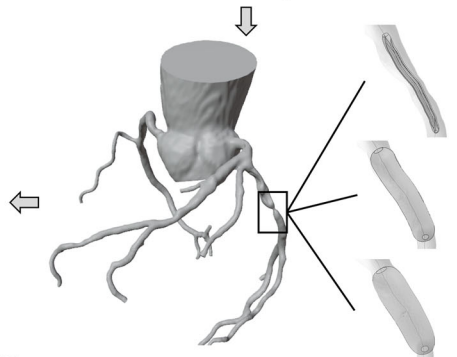
Step 2: 3D reconstructed coronary model



Step 3: Calculate Pre - PCI FFR based on coronary model



Step 5: Calculate Post - PCI FFR based on newly created coronary artery model from Step 4



Step 4: Stent-attached balloon deployment and expansion simulation

Fig. 1 | Workflow of patient-specific computational virtual coronary intervention (VCI) framework, overall steps required for the calculation of post-PCI CT fractional flow reserve (CT-FFR) and risk evaluations. The coronary artery model was 3D reconstructed (Step 1 and 2) based on coronary computed tomography angiogram (CCTA). The coronary model are meshed and assigned with patientspecific boundary conditions based on CCTA imaging (Step 3). The computationally

created balloon and stent are positioned in the region of vessel lesion (Step 4). Based on dynamic mesh, the stenting process is performed computationally. The newly created coronary artery model after stenting process is meshed and assigned with patient-specific boundary conditions again for the calculation of Post-PCI CT-FFR (Step 5).

therefore be solved using an implicit scheme through time. Objects such as the balloon, vessel, and stent are modeled as a mass-spring-damper system, where all the mass nodes in the model are linked with massless springs. Given the diagonal (lumped) mass-matrix  $M \in \mathbb{R}^{3m \times 3m}$ , implicit Euler time integration results in the following update rules:

$$\Delta x = h(v_n + \Delta v) \tag{2}$$

$$\Delta v = h(M^{-1}f(x_n + \Delta x, v_n + \Delta v))$$
 (3)

where h is the time interval. The force is evaluated at the end of the time step, known as Backward Euler. Equations 4 and 5 are equivalent to the following equations:

$$\Delta x_{n+1} = x_n + h v_{n+1} \tag{4}$$

$$\Delta v_{n+1} = v_n + h M^{-1} f_{n+1} \tag{5}$$

The non-linear force term can be approximated using a Taylor series. The linearization is achieved by replacing the nonlinear force term with its first-order Taylor series approximation, as shown in Eq. 6:

$$\Delta f(x_n + \Delta x, v_n + \Delta v) \approx f_n + \frac{\delta f}{\delta x} \Delta x + \frac{\delta f}{\delta v} \Delta v$$
 (6)

There is a trade-off made to use Taylor series approximation for an adequately close solution because there are indeed 2nd or higher-order time marching methods that can provide more accurate approximation but require more computation time. Then we can get the velocity update as shown in Eq. 7 by substituting  $\Delta x = h(v_n + \Delta v)$ 

$$\Delta v = hM^{-1} \left( f_n + \frac{\delta f}{\delta x} h(v_n + \Delta v) + \frac{\delta f}{\delta v} \Delta v \right)$$
 (7)

This results in a linear system as shown in equation:

$$\left(I - hM^{-1}\frac{\delta f}{\delta \nu} - h^2M^{-1}\frac{\delta f}{\delta x}\right)\Delta \nu = hM^{-1}\left(f_n + \frac{\delta f}{\delta x}\nu_n\right)$$
(8)

Where  $I \in \mathbb{R}^{3N \times 3N}$  is the identity matrix,  $\frac{\partial f}{\partial x}$  and  $\frac{\partial f}{\partial y}$  are needed for the internal forces. Internal force derivative with respect to position and velocity is required to be calculated in implicit integration. Assume  $x_{ij} = x_i - x_j$  is a normalised vector. The force  $f_x$  exerted on a vertex i from a spring connecting particles i and j can be shown in Eq. 9:

$$f_s = -k \left( \left\| x_{ij} \right\| - L \right) \hat{x}_{ij} \tag{9}$$

The derivative of force with direction is shown in Eq. 10:

$$\frac{\delta f_{s}}{\delta x_{i}} = -k \left( \left\| x_{ij} \right\| - L \right) \frac{\delta x_{i}j}{\delta x_{i}} + \widehat{x_{i}j} \frac{\delta \left\| x_{ij} \right\| - L}{\delta x_{i}} \\
= -k \left( 1 - \frac{L}{\left\| x_{ij} \right\|} \left( I - \widehat{x_{i}j} \widehat{x_{i}j}^{T} \right) \right) \tag{10}$$

Also, the Jacobian  $\frac{\partial d_i}{\partial V_i} = R^{3 \times 3}$  of the damping force is shown in Eq. 11:

$$\frac{\delta d_i}{\delta v_i} = -k_d I \tag{11}$$

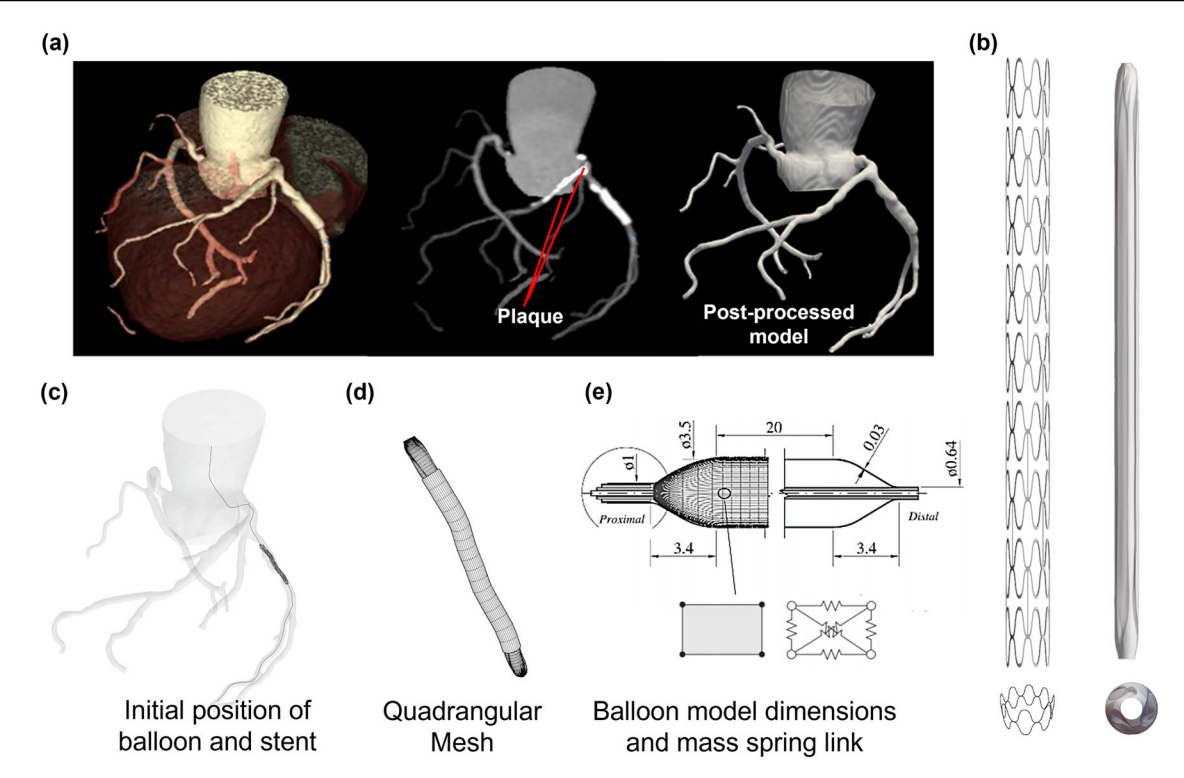


Fig. 2 | Models (coronary artery, balloon and stent) preparation for VCI framework. a 3D automated reconstruction of coronary and plaques based on CCTA dataset, the substruction of plaque mask from vessel mask gives blood mask (post-processed model) which is used for further simulations. b Balloon and stent

computationally created.  ${\bf c}$  Initial position of balloon and crimped stent surface.  ${\bf d}$  Quadrangular mesh of balloon and stent.  ${\bf e}$  The dimensions of balloon and masslink used to reconstruct the models.

Using these equations, the net Jacobians can be obtained by summing up all the elements yielding 3 N x 3 N sized matrices. The Conjugate Gradient (CG) algorithm takes a symmetric positive semi-definite matrix A, a symmetric positive definite preconditioning matrix P of the same dimension as A, a vector b and iteratively solves  $A\Delta v = B$ . The conjugate gradient method used can be described as:

$$\begin{split} \Delta \mathbf{v} = & \mathbf{z} \\ & \boldsymbol{\delta}_{0} = \text{filter}(\mathbf{b})^{T} \mathbf{P} \text{filter}(\mathbf{b}) \\ & \mathbf{r} = \text{filter}(\mathbf{b} - \mathbf{A} \Delta \mathbf{v}) \\ & \mathbf{c} = \text{filter}(\mathbf{P}^{-1} \mathbf{r}) \\ & \boldsymbol{\delta}_{\text{new}} = & \mathbf{r}^{T} \mathbf{c} \\ & \text{while } \boldsymbol{\delta}_{\text{new}} > & \boldsymbol{\epsilon}^{2} \boldsymbol{\delta}_{0} \\ & \mathbf{q} = & \text{filter}(\mathbf{A} \mathbf{c}) \\ & \boldsymbol{\alpha} = & \boldsymbol{\delta}_{\text{new}} / (\mathbf{c}^{T} \mathbf{q}) \\ & \Delta \mathbf{v} = & \Delta \mathbf{v} + \boldsymbol{\alpha} \mathbf{c} \\ & \mathbf{r} = & \mathbf{r} - \boldsymbol{\alpha} \mathbf{q} \\ & \mathbf{s} = & \mathbf{P}^{-1} \mathbf{r} \\ & \boldsymbol{\delta}_{\text{old}} = & \boldsymbol{\delta}_{\text{new}} \\ & \boldsymbol{\delta}_{\text{new}} = & \mathbf{r}^{T} \mathbf{s} \\ & \mathbf{c} = & \text{filter} \left( \mathbf{s} + & \frac{\boldsymbol{\delta}_{\text{new}}}{\boldsymbol{\delta}_{\text{old}}} \mathbf{c} \right) \end{split}$$

$$(12)$$

Steps 5 and 15 in algorithm 3.14 maintain the invariant by filtering c before adding it to  $\Delta v$ . The stopping criterion is based on  $\Delta b^T$  Pb in line 3. The vector r measures the solution error  $b-A\Delta v$ , and should not include error due to the constraints; hence filtering is added in steps 4 and 8. This conjugate gradient method was first proposed in work by Baraff and Witkin<sup>23</sup> and implemented in Visual Studio 2020 and Blender.

#### **Determining system parameters for model**

To accurately model the behavior of balloons, stents, and vessels under specific force conditions, the system parameter (k) is calculated in a manner that mimics the Finite Element Analysis (FEA) approach, as established in previous studies<sup>24,25</sup>. The equation can be shown below:

$$k^{\text{edge}} = \frac{\lambda}{3} + \frac{\mu}{2} \tag{13}$$

$$k^{\text{diag}} = \frac{5\lambda}{12} + \frac{3\mu}{4} \tag{14}$$

With Lamé constants:

$$\mu = G = \frac{E}{2(1+\nu)} \tag{15}$$

$$\lambda = \frac{E\nu}{(1+\nu)(1-2\nu)} \tag{16}$$

The damping coefficient is determined based on the work by  $^{26,27}$ . Consider a simple mass-spring-damper system consisting of two nodes with masses  $m_1$  and  $m_2$ , where the total mass is denoted as  $m=m_1+m_1$ . These nodes are connected by a spring with a stiffness constant k and a rest length  $l_0$ . When the mass-spring-damper system is subject to external forces, the damping ratio  $\zeta$  can be used to analyse the complex oscillations occurring within the springs  $^{28}$  Critical damping is employed in the fast stent deployment system to prevent unnecessary oscillations and stabilize the system as quickly as possible  $^{24}$ .

$$d = 2\frac{\sqrt{k(m_1 + m_2)}}{l_0} \tag{17}$$

The mass (m) of each vertex is determined approximately by dividing the total mass of objects by the total number of vertices. System parameters such as m, k and damping coefficients can be assigned to the VVI framework developed in Visual Studio 2020 (Microsoft, Albuquerque, New Mexico, USA) in C++. Blender (Blender Foundation, Amsterdam, The Netherlands) modules are then used for the rendering of simulation results and output model as STL (Stereolithography) file.

#### **Collision handling**

There are three aspects to collision management: bounding volume hierarchies, fast collision detection, and collision response. The computer graphics (CG) community has developed robust and efficient collision detection algorithms, and in this work, we provide a brief introduction to one such algorithm. More detailed information can be found in the works<sup>25</sup>. Our approach involves representing the 3D collision objects in a hierarchical fashion using bounding volume hierarchies (BVH) to effectively filter out the majority of non-colliding pairs of elements. We then check the distance between each pair of segments in neighboring cells. If the distance d between two segments of the discrete surgical thread is smaller than a constant value d < a, we define that the collision is detected.

Another challenge lies in collision response algorithms, which can be classified into three major categories  $^{29,30}$ : impulse-based methods  $^{31}$ , constraint-based formulations  $^{32,33}$  and penalty-based methods  $^{34}$ . In general, impulse-based methods are more suitable for rigid body collision response due to the requirement of precise dynamic collision detection at each time step. Constraint-based methods result in a more plausible simulation at the cost of additional computation  $^{35,36}$ . Traditional penalty-based methods, which are the easiest to implement, unfortunately suffer from various issues such as the jitter effect. Tang et al.  $^{29}$  proposed a continuous penalty force model for rigid body collisions. Wang et al.  $^{37}$  improved upon the penalty method by introducing a continuous penalty averaged force model for real-time application in soft objects. We adapt this approach in our VCI framework. The continuous penalty force created by the collision during the time interval  $\Delta t$  is:

$$\mathbf{F}_{ef} = \frac{\mathbf{I}}{\Delta t} = \frac{1}{\Delta t} \int_{t}^{t+\Delta t} \mathbf{F}_{pf}(t) dt \tag{18}$$

$$\mathbf{F}_{pf}(t) = K(\Delta d - |\mathbf{d}(t)|) \frac{\mathbf{d}(t)}{|\mathbf{d}(t)|}$$
(19)

where K is a stiffness constant,  $\mathbf{F}_{pf}(t)$  represent the penalty force created at time t and  $\mathbf{I} = \int_t^{t+\Delta t} \mathbf{F}_{pf}(t) dt$  is the impulse produced by the penalty force  $\mathbf{F}_{pf}(t)$  during time interval  $[t, t + \Delta t]$ . The continuous penalty force can essentially be taken as the average of the penalty force during a time interval.

#### **Balloon expansion**

The expansion of a virtual folded balloon is achieved by applying realistic internal pressure perpendicular to the surface of the balloon, with the pressure distributed to each vertex of the balloon. Additionally, virtual folded balloons based on manufacturers' guidance and a cylindrical structure with the size of crimped stents were created and discretized with a quadrangular mesh (Fig. 2d), then stored for usage.

The equilibrium state of the balloon is achieved by balancing the internal force and the counterforce generated by mass links at each vertex of the quadrangular mesh. The accuracy of balloon expansion is ensured by an expansion test that compares the balloon diameter in the equilibrium state to the balloon manufacturers' guidance. Regarding the stent, the cylindrical structure represents the crimped stent in its initial configuration, and the simulation of stent implantation is performed by attaching the stent to a balloon of suitable size. Although the structure of the stent can be mapped onto the cylindrical surface, it does not affect the simulation results, and detailed flow analysis in the stented vessel is not included within the scope of this manuscript. For visualization purposes, a stent was manually created as shown in Fig. 2b.

The simulation of balloon angioplasty and stent implementation was conducted within the VCI framework, which incorporates clinical settings during the PCI procedure, such as balloon size, balloon location, balloon internal pressure, stent size, and stent position. The centerline of the coronary vessel was extracted and imported into the VCI graphical user interface. The operator can maneuver the devices to the region of interest, as depicted in Fig. 2c. Within the VCI graphical user interface, the operator selects and specifies the desired length and diameter of the stent and balloon to be deployed, as shown in Supplemental Fig. 3.

To ensure mophylogical accuracy, the VCI framework maintains force equilibrium during balloon expansion and stent deployment, balancing internal force and external force. The post-PCI vessel morphology (e.g., cross-sectional area, curvature, and lumen expansion) is computed using the dynamic mesh solver, ensuring force balance at each iteration. The final deformed vessel geometry is then used in computational fluid dynamics (CFD) simulations to derive the post-PCI fractional flow reserve (CT-FFR)<sup>38</sup>.

#### Computational fluid dynamic settings and hemodynamic studies

The coronary artery models, including pre-PCI CTA-reconstructed models, post-PCI CTA-reconstructed models, and corresponding VCI-simulated models, were meshed using CFD-VisCART (ESI Group, Paris, France), employing a stair-step conforming unstructured mesh of the Omnitree Cartesian tree type. Blood flow, assumed to be incompressible, was modeled using the incompressible 3D Navier-Stokes equations solved via the finite volume approach in CFD-ACE+ (ESI Group, Paris, France), with a central differencing scheme for spatial interpolations. The SIMPLE Consistent (SIMPLEC) pressure correction method<sup>39,40</sup> and an algebraic multigrid method for convergence acceleration<sup>41</sup> were used. The flow was assumed to be laminar and blood was modelled as a homogenous and Newtonian fluid with its density and dynamic viscosity of 1060 kg/m<sup>3</sup> and 0.004 Pa·s, respectively. For all cases (Pre-PCI CTA-reconstructed models, post-PCI CTA-reconstructed models, and corresponding VCI-simulated models), the vessel wall was approximated as rigid, with non-slip boundary conditions applied. Cardiac-induced wall motion was not incorporated.

In the VCI framework, steady-state BCs are used for the calculation of CT-FFR. This is based on two reasons. First, the calculation of invasive CT-FFR is based on time-averaged pressure measured over several cardiac cycles. Second, using steady-state BC reduce the computational cost, without losing the predictability of CT-FFR as shown in studies <sup>42,43</sup>. The model of calculating CT-FFR is based on left ventricular mass (LVM) based mode. The LVM model quantifies total hyperemic coronary blood flow based on LVM and distributes outlet coronary blood flow based on outlet diameter. Based on the LVM measured from the workstation (CoronaryDoc, Shukun Technology, Beijing, China), the resting state flow Qrest in the right and left coronary branches is calculated as:

$$Q_{\text{rest}} = Y_0 \times LVM^{0.75} \tag{20}$$

where  $Y_0$  is a normalisation constant of 0.71<sup>44</sup>. The coronary blood flow value in the rest state (Qrest) is assumed to be 16%<sup>42</sup> of that in the hyperemic state. Qhyp can be calculated as:

$$Q_{hyp} = \frac{Q_{rest}}{TCRI} \tag{21}$$

TCRI is the hyperemic factor, and TCRI is  $0.16^{43}$ . Murray's law between vessel radius is applied. The flow in the coronary branch at ith outlet  $Q_{\text{out},i}^{hyp}$  can be calculated according to the following equation:

$$Q_{\text{out},i}^{hyp} = \frac{D_i^{\beta}}{\sum_{i=1}^{n} \times D_i^{\beta}}$$
 (22)

where  $\beta$  is 2.55,  $D_i$  is the diameter of each branch outlet, and n is the number of branch outlets<sup>45</sup>. The coronary outlet pressure is set to MAP (MAP =

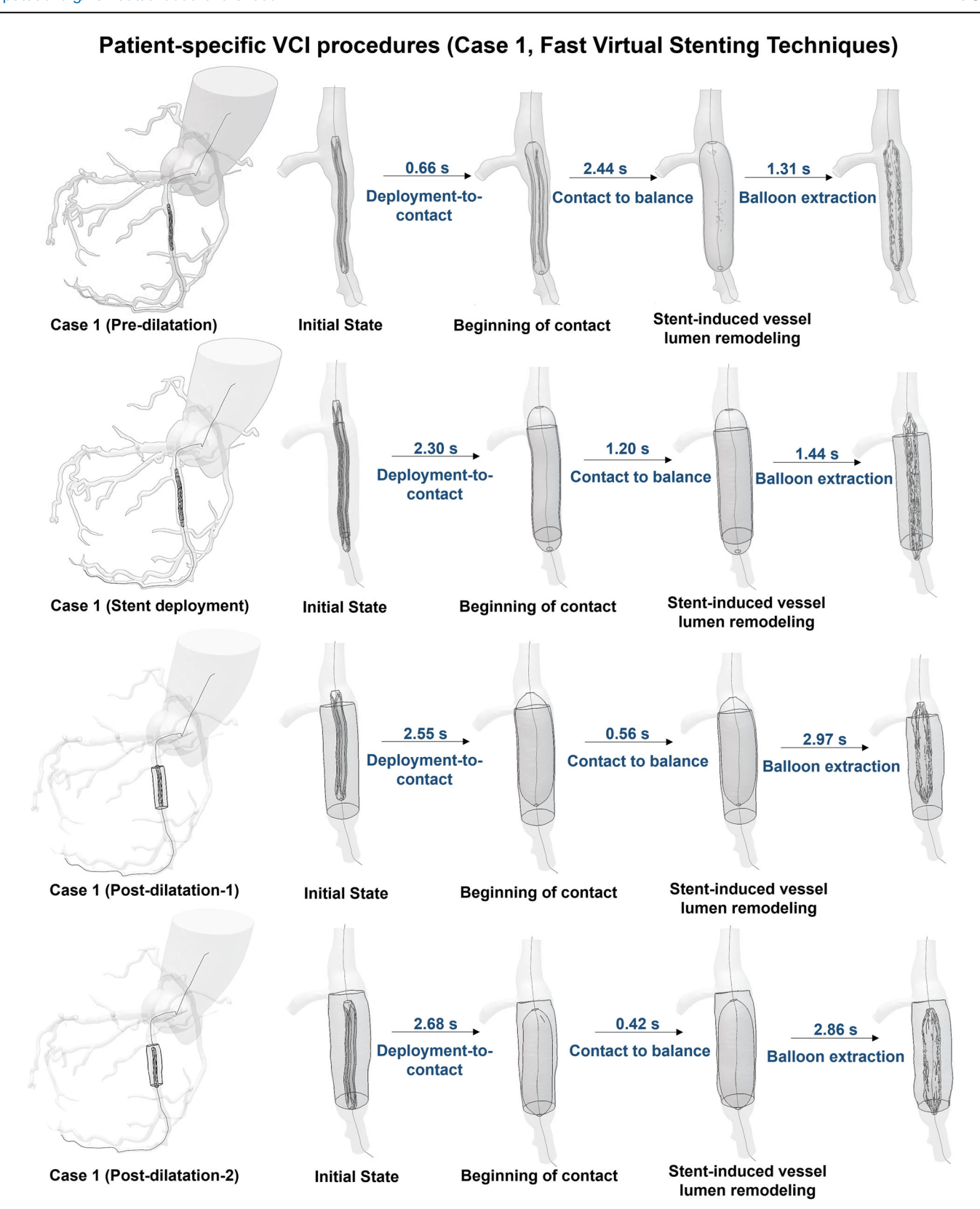


Fig. 3 | Fast virtual stenting technique for representative case. Four steps are included in the clinical process: pre-dilatation, stent deployment, post-dilatation-1, and post-dilatation-2. We replicated computationally all the steps of the stenting procedure within VCI framework. Three stages are included in each step and the

computation time is rapid. For each clinical procedure, there are three main states: initial states, beginning of contact and stent-induced vessel lumen remodeling states (n = 1 representative case).

 $0.4*(SBP-DBP) + DBP)^{46}$  where SBP and DBP are brachial systolic and diastolic blood pressure provided by CoronaryDoc, Shukun Technology, Beijing, China. The coronary artery resistance  $R_{\text{out},i}^{\text{hyp}}$  can be calculated as:

$$R_{\text{out},i}^{\text{hyp}} = \frac{MAP - P_{\nu}}{Q_{\text{out},i}^{\text{hyp}}}$$
 (23)

where  $R_{{
m out},i}^{{
m hyp}}$  is the resistance of ith outlets,  $P_{\nu}$  is assume to be 5 mmHg¹. The same boundary conditions were assigned for each patient case (post-PCI CTA-reconstructed models and the corresponding VCI-simulated models) at the inlet and outlets. Convergence criteria of absolute and relative residual reductions of  $1\times 10^{-8}$  and  $1\times 10^{-5}$  were imposed respectively, with convergence typically reached in fewer than 100 iterations.

#### **Comparison metrics**

The post-VCI CT-FFR, post-VCI lumen, and post-VCI curvature were compared to the post-PCI CT-FFR, post-PCI lumen, and post-PCI curvature segmented from CCTA. The metrics from post-PCI CCTA were used as a reference. The mean lumen cross-sectional area (CSA), post-CT-FFR, and curvature across the stented segment—including approximately 2 mm of vessel immediately proximal and distal to the stent—were used as comparison metrics.

#### Statistics and reproducibility

Statistical analysis was performed with the statistical package MedCalc® Statistical Software version 20.116 (MedCalc Software Ltd, Ostend, Belgium). Continuous variables were expressed as mean ± standard error of the mean. The main aim was to access the agreement between post-VCI CT-FFR and post-PCI CT-FFR by using the Bland-Altman method, other metrics such as lumen cross-sectional area and curvature over the stented segment plus ~2 mm proximal and distal margins were also assessed using the Bland-Altman method. The metric of accuracy is defined by the mean difference and the precision is defined as the standard deviation (SD) of the mean.

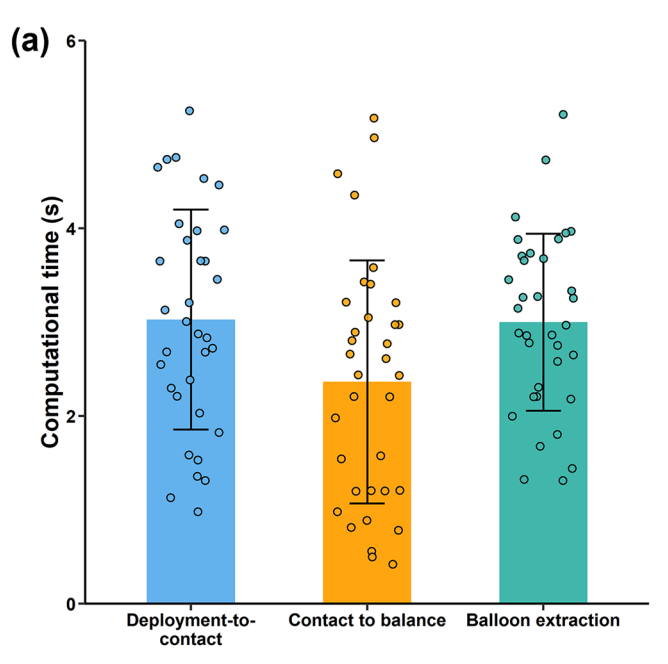
A total of 30 patients were initially screened; 21 met the inclusion criteria, of which 9 patients (9 vessels) were included in the final analysis. Each virtual coronary intervention (VCI) simulation was performed once per vessel using a standardized pipeline. No technical or biological replicates were applicable due to the retrospective and imaging-based nature of the study. Reproducibility was assessed by comparing VCI predictions with post-procedural CTA-derived anatomical and physiological measurements.

#### Reporting summary

Further information on research design is available in the Nature Portfolio Reporting Summary linked to this article.

#### Results Efficiency of VCI

All the computations were executed in Visual Studio C + + on one 11th Gen Intel(R) Core (TM) i7-11800H CPU @ 2.30 GHz processor with 32GB of RAM. Simulation of a complete PCI process consists of three steps: predilatation (PRE), stent-deployment (DEPLOY), and post-dilatation (POST). Each step involved three stages: deployment-to-contact (Stage 1), contact-to-balance (Stage 2), and balloon-extraction (Stage 3). Figure 3 shows the simulation for one representative case which includes all predilatation, stent deployment, and post-dilatation steps. It takes a few seconds to compute each step on a single CPU. For the 10 successfully treated cases, the mean computing times for PRE, DEPLOY and POST processes were  $7.83 \pm 2.38$  s,  $8.50 \pm 2.81$  s and  $8.39 \pm 1.70$  s. The mean computational times for Stage-1, Stage-2 and Stage-3 were  $8.79 \pm 1.02$  s,  $6.96 \pm 1.11$  s and  $9.17 \pm 0.89$  s as it can be seen in Fig. 4, and the overall simulation time for virtual stenting was  $24.92 \pm 1.00$  s.



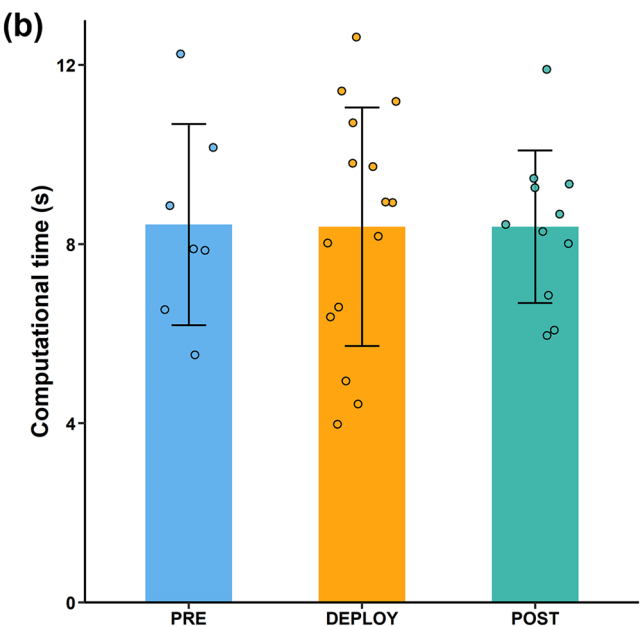


**Fig. 4** | Computational time for fast virtual stenting technique. a Computing time for different stages during virtual stenting for all the simulated cases (n = 9), there are deployment-to-contact, contact-to-balance and balloon extraction stages. **b** Computing time for virtual balloon pre-dilatation (PRE), stent-deployment (DEPLOY), and balloon post-dilatation (POST) for all the simulated cases (n = 9).

#### Accuracy of the VCI

Figure 5a, b show both the pre-PCI and post-VCI LAD vessel, lesion vessel cross-section view and calculated CT-FFR based on CCTA reconstruction. The accuracy of VCI was accessed mainly based on CT-FFR by comparing post-VCI CT-FFR to the real post-PI CT-FFR CTA-reference models (CTA model) as illustrated in Fig. 5c, d. The calculated post-PCI CT-FFR was  $0.92\pm0.09$  and the predicted post-VCI CT-FFR was  $0.90\pm0.08$  (mean difference:  $-0.02\pm0.05$  FFR unit; limits of agreement: -0.08 to 0.05) (Fig. 5e, f). For morphological analysis, CSA and luminal curvature were compared over the stented segment plus ~2 mm proximal and distal margins (Fig. 6a). Slices perpendicular to the centreline were extracted across this extended region (Fig. 6b). CSAs (Area  $_{\rm n}$ , n=1 - N) (N was in the

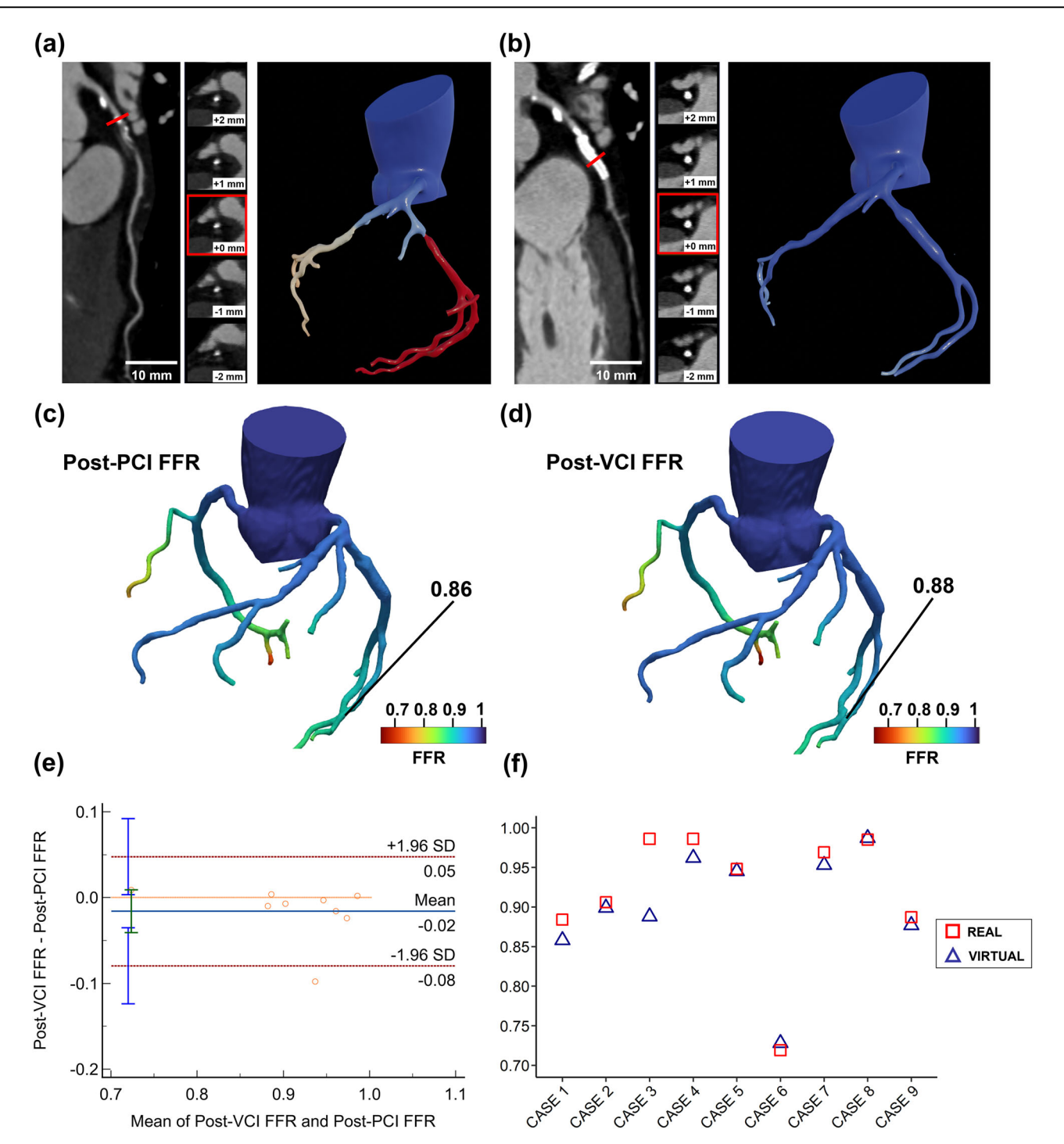


Fig. 5 | Validation of VCI framework with regard to post-PCI CT-FFR prediction. a Pre-PCI left anterior descending (LAD) artery as reconstructed from coronary CTA, including cross-sectional slices (red box indicating calcified plaque). The pre-PCI CT-FFR at the distal LAD was computed to be 0.67. b Post-PCI reference model showing the implanted stent (bright signal due to "blooming").

artifact") on the same LAD artery, along with the post-PCI FFR measurement of 0.88. **c**, **d** Post-VCI CT-FFR and Post PCI CT-FFR, the predicted post-VCI CT-FFR is 0.86 at distal LAD and reference Post PCI CT-FFR is 0.88 at same probe location for one representative case. **e**, **f** Statistical results for the comparison between Post-VCI CT-FFR and Post PCI CT-FFR (n = 9 vessels).

scope of 60–100, due to the different lengths of the stented vessel) were compared between the VCI simulation and CTA-reference outcomes, as:

$$Diff^{A} = \left| \frac{\left( Area_{n}^{VCI} - Area_{n}^{PCI} \right)}{Area_{n}^{PCI}} \right|$$
 (24)

Besides, luminal curvature of the  $n^{th}$  points along the centreline (Cn, n = 1-N) was evaluated by computing:

$$Diff^{C} = \left| \frac{\left( C^{VCI} - C^{PCI} \right)}{C^{PCI}} \right| \tag{25}$$

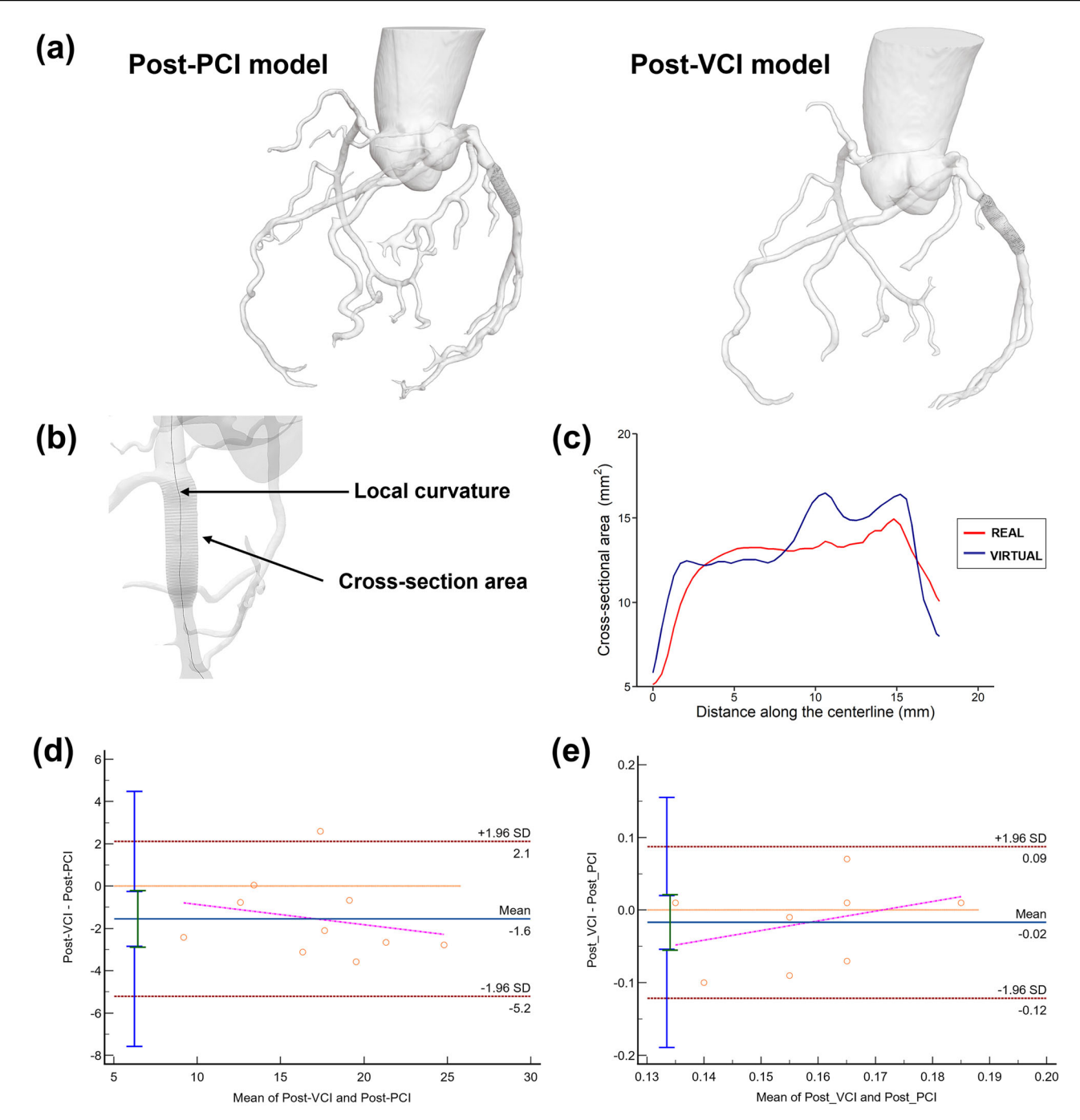


Fig. 6 | Validation of VCI framework for curvature and crosse section prediction. a Crosse section analysis region across the stented segment and  $\sim$ 2 mm vessel cuffs from post-PCI model and post-VCI model. b local curvature and crosse section slicers were extracted. c The line graph that shows comparison of extracted cross-

sectional area (CSA) from post-PCI model and post-VCI model in one representative case.  $\mathbf{d}$ ,  $\mathbf{e}$  Statistical results for both CSA and curvature among all simulated cases (n=9 vessels).

Figure 6c shows comparison of extracted cross-sectional area (CSA) from post-PCI model and post-VCI model in one representative case. The predicted post-VCI CSA is  $16.356 \pm 4.409 \text{ mm}^2$  and post-PCI CSA is  $17.91 \pm 4.84 \text{ mm}^2$  (mean difference:  $-1.55 \pm 1.89 \text{ mm}^2$ ; limits of agreement: -5.22 to 2.12) (Fig. 6d), the predicted centreline curvature of stented region is  $0.15 \pm 0.04 \text{ mm}^{-1}$  and post centreline curvature is  $0.17 \pm 0.03 \text{ mm}^{-1}$  (mean difference:  $-0.02 \pm 0.06 \text{ mm}^{-1}$ ; limits of agreement: -0.12 to 0.09) (Fig. 6e). The accuracy of the VCI was stratified according to the morphological parameter as well as hemodynamic parameter.

#### Discussion

In this study, we proposed and validated a patient-specific VCI technique. The main results suggest the proposed VCI technique can predict post-PCI CT-FFR with high accuracy. The predicted post-VCI CT-FFR was close to the post-PCI CT-FFR derived from CCTA after PCI. Moreover, the evaluation of morphological parameters (CSA and centreline curvature) demonstrated the rapid VCI prediction is consistent with actual PCI results. In this study, a mean of  $24.92 \pm 1.00$  s was used on a single processor for the fast coronary stenting simulation, which in most cases (n=8) consists of three steps (PRE, DEPLOY and POST). Previous 3D computational stent-

induced coronary vessel remodelling studies were mainly based on the FEM for structural analysis which is not suitable for clinical use due to its high computation requirement<sup>47–49</sup>.

Although the fast VCI simulated by using a cubic spline to adjust the cross-sectional diameters to smooth the vessel trajectory based on the size (diameter and length) of the stent proposed by<sup>50,51</sup>, this radius correction virtual stenting method can achieve rapid computation of stenting process, the accuracy of such methods might not be insured for the accurate anatomical assessment. The radius correction virtual stenting method might not be ensured for cases of severely calcified vessels, bifurcation stenosis, or aortic-ostial lesions, severe vessel tortuosity, previous revascularization, and in patients with atrial fibrillation, etc<sup>1</sup>. It is important to note that, for patients with pre-PCI CT-FFR less than 0.80, above mentioned scenario occurs frequently. On the contrary, the VCI method can provide a more realistic prediction of morphological outcomes which has the potential to address the above-mentioned challenges.

A more realistic VCI like the one developed in this study that can simulate multiple stent deployment and can adapt to various vessel conditions is therefore required to address the mentioned challenges. Compared to previous coronary stenting algorithms<sup>47–51</sup>, the VCI developed in this work has the following advantages:

- 1. The ability to realise complex PCI simulations with rapid computation. As can be seen in Fig. 7 two stents were deployed to the bifurcation site known as the culotte technique. In this case, a stent is first developed to the main branch (MV), and the first proximal optimisation technique is applied to the 1st stent to ensure the full expansion of the 1st stent, the 2nd stent is delivered and deployed in the side branch (SB) before side branch structure opening process. The second proximal optimisation technique is used to ensure the contact of 2nd stent with MV. Finally, kissing balloon inflation is performed to avoid the obstruction of the bifurcation vessel. This benchcase shows the potential of VIC to perform complete PCI procedures such as the culotte technique.
- 2. The ability to simulate pre-dilatation and post-dilatation in real-time with balloon expansion. Pre and post-dilatation process was simulated

- in the actual PCI among 7 cases and simulated within the VCI framework proposed. Most of the previous fast VCIs neglected predilatation and post-dilatation which can affect the accuracy of predicted result as it can be seen in the Fig. 8, the predicted Post-RC CT-FFR is 0.86 with only stent implation process. Whereas the predicted Post-VCI CT-FFR from the VCI method that contatin predilation and then stent implantation process is 0.88 which is closer to the Post-PCI CT-FFR -0.89.
- 3. The potential to simulate various vessel conditions. In the previous FE study, the plaque can be simulated by the stress-strain graph based on the constitutive equation with multiple coefficients<sup>14</sup>. A similar idea can be applied to the fast coronary stent deployment algorithm proposed in this study by changing the vessel material parameters, further investigation should be carried out to export the potential of algorithms to mimic different vessel properties. The ability to simulate two-stent techniques in the bifurcation of coronary such as the double kissing crush technique and culotte technique should be examined further.

The study has its own limitations. The key limitations are: (1) the number of cases analysed in this proof-of-concept study is modest due to the exclusion of cases with complex coronary geometries. Future studies are expected to incorporate a broader range of cases, including complex anatomies (various lesion location, lesion morphology, tissure characteristics) and acute presentations. Additionally, the retrospective nature of the study limited access to routine post-PCI invasive FFR measurements, preventing direct validation against the gold standard. (2) the movement of vessels during the cardiac cycle was not considered. (4D simulation) with time make the simulation accurate at the expense of computation time; (3) detailed mechanical contact models<sup>21</sup>, patient-specific plaque mechanics (e.g., via CT attenuation thresholds or OCT-derived stress–strain data), and explicit stent structure to improve predictions of incomplete expansion and post-PCI hemodynamics should be incorporated in the future; (4) invasive

## Patient-specific novel fast virtual coronary stenting (Bench case – Culotte technique)

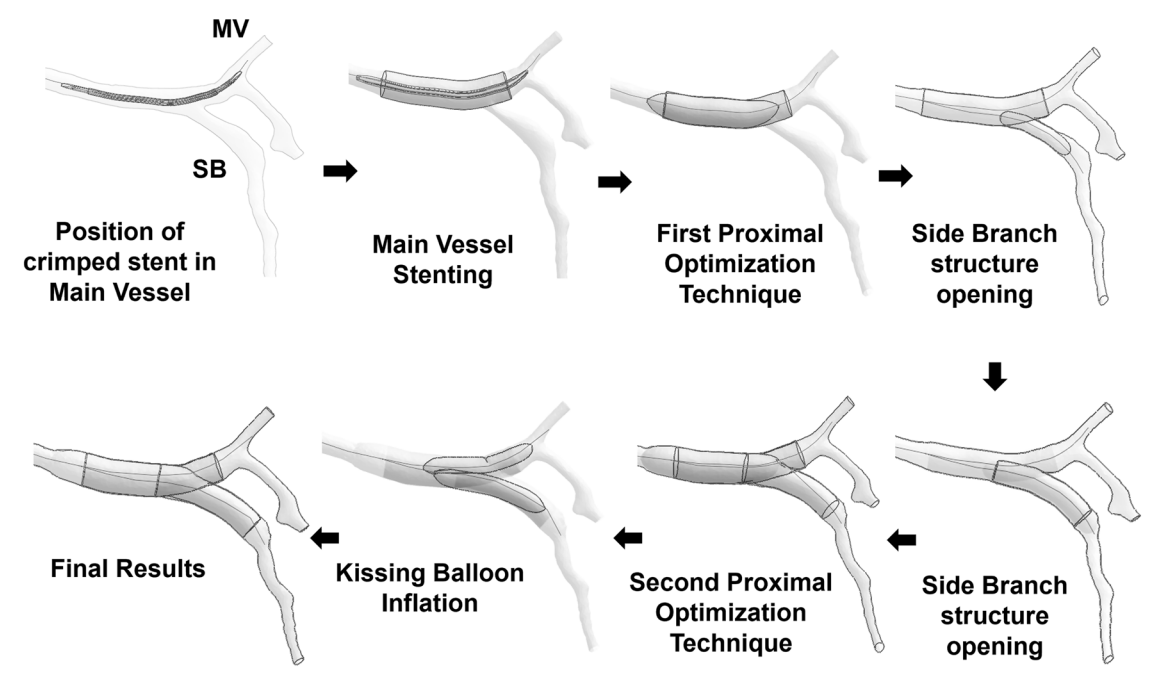
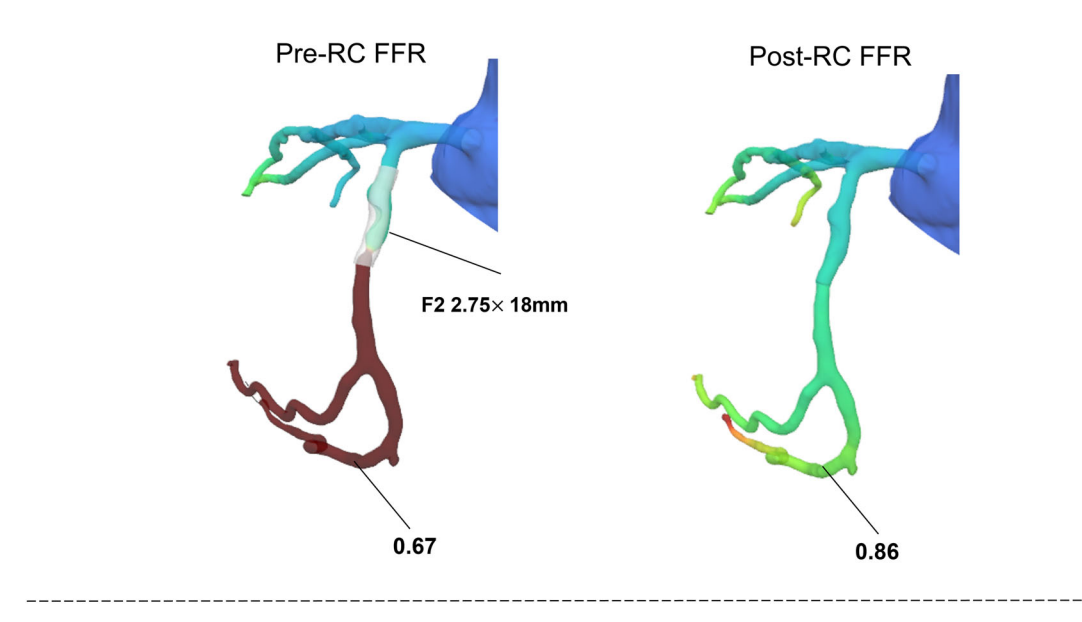


Fig. 7 | A patient-specific coronary bifurcation geometry was stented with the two stents using Culotte technique.

#### Direct Virtual Stent Implementation with Radius Correction (RC) Method



#### Pre-Dilatation + Stent deployment with Virtual Coronary Invention (VCI) Method

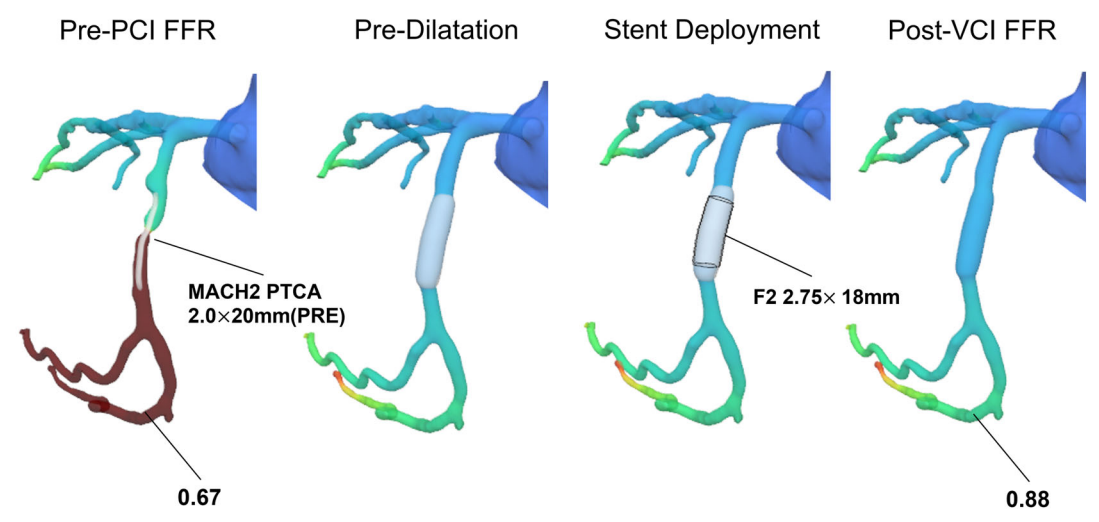


Fig. 8 | The comparision between direction stent implantation with RC method and VCI method that contain pre-dilatation and stent implantation steps (n = 9 cases).

measurement should be used for the validation of CT-FFR and OCT should be used for the validation of plaque segmentation. More validation should be carried out if the relevant data is available.

#### **Conclusions**

Non-invasive physiological assessment (post-PCI CT-FFR prediction) and anatomical assessment (detailed coronary stenting simulation) can facilitate pre-procedural planning of PCI by evaluating the degree of functional revascularization and predicting stented coronary vessels. The VCI framework proposed in this work achieved physiological assessment by accurately predicting post-PCI CT-FFR, and anatomical assessment by simulating detailed stenting procedures in real-time.

The present framework could contribute to functional coronary angiography (FCA) derived from computed angiograms to facilitate non-invasive PCI planning and the present framework has the protentional to assist in improving the efficacy and safety of PCI by performing complex interventions in real time.

#### Data availability

The DICOM imaging data used in this study are not publicly available due to patient privacy regulations but may be available from the corresponding author upon reasonable request and with approval from the institutional review board. The numerical source data that support the plots in this article are provided as separate Excel files and described as Supplementary Data. Specifically, the source data for Fig. 4a, b are in Supplementary Data 1; the source data for Fig. 5c–f are in Supplementary Data 2; and the source data for Fig. 6c–e are in Supplementary Data 3. Additional clarification can be obtained from the corresponding author, Dr Mengzhe Lyu (ucemmly@ucl.ac.uk).

#### Code availability

The custom code developed for this study is subject to institutional policy and ongoing intellectual-property review, and therefore cannot be released publicly at this time. A comprehensive description of the algorithms, modelling workflow, and parameter settings is provided in the *Methods* 

section. Researchers who require additional clarification may contact the corresponding author, Dr. Mengzhe Lyu (email: ucemmly@ucl.ac.uk), to discuss the possibility of limited, non-commercial access under a data-use agreement.

Received: 31 July 2024; Accepted: 18 July 2025; Published online: 25 August 2025

#### References

- Sonck, J. et al. Clinical Validation of a Virtual Planner for Coronary Interventions Based on Coronary CT Angiography. *JACC:* Cardiovasc. Imaging 15, 1242–1255 (2022).
- Li, S.-J. et al. Cutoff Value and Long-Term Prediction of Clinical Events by FFR Measured Immediately After Implantation of a Drug-Eluting Stent in Patients With Coronary Artery Disease. *JACC: Cardiovasc. Interventions* 10, 986–995 (2017).
- Sedlis, S. P. & Lorin, J. D. Should Fractional Flow Reserve Be Measured After Stent Deployment? Routinely? Ever?\*. JACC: Cardiovasc. Interventions 10, 996–998 (2017).
- Agarwal, S. K. et al. Clinical and angiographic predictors of persistently ischemic fractional flow reserve after percutaneous revascularization. Am. Heart J. 184, 10–16 (2017).
- Collison, D. et al. Post-stenting fractional flow reserve vs coronary angiography for optimization of percutaneous coronary intervention (TARGET-FFR). Eur. Heart J. 42, 4656–4668 (2021).
- Mallidi, J. et al. Long-term outcomes following fractional flow reserveguided treatment of angiographically ambiguous left main coronary artery disease: A meta-analysis of prospective cohort studies. Catheterization Cardiovasc. Interventions 86, 12–18 (2015).
- Johnson, N. P. et al. Prognostic Value of Fractional Flow Reserve: Linking Physiologic Severity to Clinical Outcomes. *J. Am. Coll. Cardiol.* 64, 1641–1654 (2014).
- Piroth, Z. et al. Prognostic Value of Fractional Flow Reserve Measured Immediately After Drug-Eluting Stent Implantation. *Circulation:* Cardiovasc. Interventions 10, e005233 (2017).
- Doll, J. A. et al. Management of Percutaneous Coronary Intervention Complications. *Circulation: Cardiovasc. Interventions* 13, e008962 (2020).
- Bauer, T. et al. Fate of Patients With Coronary Perforation Complicating Percutaneous Coronary Intervention (from the Euro Heart Survey Percutaneous Coronary Intervention Registry). Am. J. Cardiol. 116, 1363–1367 (2015).
- Iverson, A. et al. Prevalence, Trends, and Outcomes of Higher-Risk Percutaneous Coronary Interventions Among Patients Without Acute Coronary Syndromes, Cardiovascular Revascularization. *Medicine* 20, 289–292 (2019).
- Fanaroff, A. C. et al. Outcomes of PCI in Relation to Procedural Characteristics and Operator Volumes in the United States. *J. Am. Coll. Cardiol.* 69, 2913–2924 (2017).
- Mortier, P. et al. Provisional Stenting of Coronary Bifurcations: Insights Into Final Kissing Balloon Post-Dilation and Stent Design by Computational Modeling. *JACC: Cardiovasc. Interventions* 7, 325–333 (2014).
- Zhao, S. et al. Patient-specific computational simulation of coronary artery bifurcation stenting. Sci. Rep. 11, 16486 (2021).
- Wu, W. et al. Three dimensional reconstruction of coronary artery stents from optical coherence tomography: experimental validation and clinical feasibility. Sci. Rep. 11, 12252 (2021).
- Gosling, R. C. et al. Virtual Coronary Intervention: A Treatment Planning Tool Based Upon the Angiogram. *JACC: Cardiovascular Imaging* 12, 865–872 (2019).
- Lyu, M. In-silico virtual planning of vascular interventional procedures, Ph.D. dissertation, University College London (UCL), London, U.K. Available: https://discovery.ucl.ac.uk/id/eprint/10190900 (2024).

- Chen, M. et al. Diagnostic performance of deep learning-based vascular extraction and stenosis detection technique for coronary artery disease. Br. J. Radio. 93. 20191028 (2020).
- Nochetto, R. H., Paolini, M. & Verdi, C. A Dynamic Mesh Algorithm for Curvature Dependent Evolving Interfaces. *J. Computational Phys.* 123, 296–310 (1996).
- Lyu, M., Ventikos, Y., Peach, T.W. Makalanda, L. & Bhogal, P. Virtual Flow-T Stenting for Two Patient-Specific Bifurcation Aneurysms, Front. Neurol. 12. https://www.frontiersin.org/articles/10.3389/fneur. 2021.726980 (2021).
- Chen, D. et al. Virtual stenting with simplex mesh and mechanical contact analysis for real-time planning of thoracic endovascular aortic repair. *Theranostics* 8, 5758–5771 (2018).
- Lyu, M. et al. Treatment for middle cerebral artery bifurcation aneurysms: in silico comparison of the novel Contour device and conventional flow-diverters, *Biomech. Model. Mechanobiol.* early access, https://doi.org/10.1007/s10237-024-01829-3 (2024).
- Lyu, M. et al. A novel computational pre-procedural planning model for coronary interventions based on coronary CT angiography, bioRxiv, preprint, Jul. 29 2024, https://doi.org/10.1101/2024.07.29. 605713.
- 24. Tuplin, W. A. The Mechanics of Vibration. *Nature* **192**, 844–845 (1961).
- 25. Coumans, E., Bai, Y. Pybullet, a python module for physics simulation for games, robotics and machine learning, http://pybullet.org/ (2016).
- Natsupakpong, S. & Cenk Çavuşoğlu, M. Determination of elasticity parameters in lumped element (mass-spring) models of deformable objects. *Graph. Models* 72, 61–73 (2010).
- Zhang, J., Zhong, Y. & Gu, C. Deformable Models for Surgical Simulation: A Survey. *IEEE Rev. Biomed. Eng.* 11, 143–164 (2018).
- Lloyd, B., Szekely, G. & Harders, M. Identification of Spring Parameters for Deformable Object Simulation. *IEEE Trans. Vis. Computer Graph.* 13, 1081–1094 (2007).
- 29. Tang, M., Manocha, D., Otaduy, M. A. & Tong, R. Continuous penalty forces. ACM Trans. Graph. 31, 107:1–107:9 (2012).
- Witkin, A. Physically based modeling: principles and practice constrained dynamics. Computer Graph. 9, 27 (1997).
- Mirtich, B., Canny, J. Impulse-based simulation of rigid bodies, in: Proceedings of the 1995 Symposium on Interactive 3D Graphics, Association for Computing Machinery, New York, NY, USA, 1995: p. 181-ff.
- Bridson, R., Fedkiw, R. & Anderson, J. Robust treatment of collisions, contact and friction for cloth animation. *ACM Trans. Graph.* 21, 594–603 (2002).
- Duriez, C., Dubois, F., Kheddar, A. & Andriot, C. Realistic haptic rendering of interacting deformable objects in virtual environments. *IEEE Trans. Vis. Computer Graph.* 12, 36–47 (2006).
- Wriggers, P., Vu Van, T. & Stein, E. Finite element formulation of large deformation impact-contact problems with friction. *Computers* Struct. 37, 319–331 (1990).
- Hüsken, N. Realtime Simulation of Stiff Threads for microsurgery training simulation, https://doi.org/10.11588/HEIDOK.00017120 (2014).
- 36. Bertails-Descoubes, F., Cadoux, F., Daviet, G. & Acary, V. A nonsmooth Newton solver for capturing exact Coulomb friction in fiber assemblies. *ACM Trans. Graph.* **30**, 6:1–6:14 (2011).
- Wang, Z., Fratarcangeli, M., Ruimi, A. & Srinivasa, A. R. Real time simulation of inextensible surgical thread using a Kirchhoff rod model with force output for haptic feedback applications. *Int. J. Solids Struct.* 113–114, 192–208 (2017).
- Antiga, L. et al. An image-based modeling framework for patientspecific computational hemodynamics. *Med. Biol. Eng. Comput.* 46, 1097–1112 (2008).
- 39. Lonsdale, R. D. An Algebraic Multigrid Solver for the Navier-Stokes Equations on Unstructured Meshes. *Int. J. Numer. Methods Heat. Fluid Flow.* **3**, 3–14 (1993).

- Ni, M.-J. & Abdou, M. A. A bridge between projection methods and SIMPLE type methods for incompressible Navier–Stokes equations. *Int. J. Numer. Methods Eng.* 72, 1490–1512 (2007).
- Van Doormaal, J. P. & Raithby, G. D. Enhancements of the Simple Method for Predicting Incompressible Fluid Flows. *Numer. Heat. Transf.* 7, 147–163 (1984).
- Wilson, R. F., Wyche, K., Christensen, B. V., Zimmer, S. & Laxson, D. D. Effects of adenosine on human coronary arterial circulation. *Circulation* 82, 1595–1606 (1990).
- Schwarz, J. C. V., van Lier, M. G. J. T. B., van den Wijngaard, J. P. H. M., Siebes, M. & VanBavel, E. Topologic and Hemodynamic Characteristics of the Human Coronary Arterial. *Circulation, Front. Physiol.* 10, 1611 (2019).
- Choy, J. S. & Kassab, G. S. Scaling of Myocardial Mass to Flow and Morphometry of Coronary Arteries. *J. Appl. Physiol.* 104, 1281–1286 (2008).
- Bos, W. J. et al. How to assess mean blood pressure properly at the brachial artery level. *J. Hypertens.* 25, 751 (2007).
- Müller, L. O. et al. Impact of baseline coronary flow and its distribution on fractional flow reserve prediction. *Int. J. Numer. Methods Biomed. Eng.* 37, e3246 (2021).
- Perrin, D. et al. Patient-specific numerical simulation of stent-graft deployment: Validation on three clinical cases. *J. Biomech.* 48, 1868–1875 (2015).
- Lally, C., Dolan, F. & Prendergast, P. J. Cardiovascular stent design and vessel stresses: a finite element analysis. *J. Biomech.* 38, 1574–1581 (2005).
- Fournier, S. et al. Association of Improvement in Fractional Flow Reserve With Outcomes, Including Symptomatic Relief, After Percutaneous Coronary Intervention. *JAMA Cardiol.* 4, 370–374 (2019).
- Collet, C. et al. Implementing Coronary Computed Tomography Angiography in the Catheterization Laboratory. *JACC: Cardiovasc. Imaging* 14, 1846–1855 (2021).
- Tonino, P. A. L. et al. Fractional Flow Reserve versus Angiography for Guiding Percutaneous Coronary Intervention. *N. Engl. J. Med.* 360, 213–224 (2009).

#### **Acknowledgements**

This study is supported by the National Natural Science Foundation of China (T2425020, 62475173). The authors would like to thank Siemens Healthineers Digital Technology Co. Ltd. and Siemens Healthineers collaboration team for providing additional support.

#### **Author contributions**

M.L.: conceptualisation, data curation, formal analysis, funding acquisition, investigation, methodology, writing original manuscript, reviewing and editing; C.L.: formal analysis, investigation, methodology, reviewing and

editing; X.Z.: formal analysis, investigation, methodology, reviewing and editing; X.W.: formal analysis, investigation, methodology, reviewing and editing; Q.L.: formal analysis, writing original manuscript, reviewing and editing; R.T.: conceptualisation, formal analysis, investigation, methodology, reviewing and editing; Y.V.: conceptualisation, funding acquisition, formal analysis, investigation, supervision, reviewing and editing. D.C.: conceptualisation, funding acquisition, formal analysis, investigation, supervision, reviewing and editing.

#### **Competing interests**

The authors declare no competing interests.

#### **Additional information**

**Supplementary information** The online version contains supplementary material available at https://doi.org/10.1038/s43856-025-01055-7.

**Correspondence** and requests for materials should be addressed to Mengzhe Lyu, Ryo Torii or Duanduan Chen.

**Peer review information** *Communications Medicine* thanks Zhiyong Li, Yasutsugu Shiono and the other, anonymous, reviewer(s) for their contribution to the peer review of this work.

Reprints and permissions information is available at http://www.nature.com/reprints

**Publisher's note** Springer Nature remains neutral with regard to jurisdictional claims in published maps and institutional affiliations.

Open Access This article is licensed under a Creative Commons Attribution-NonCommercial-NoDerivatives 4.0 International License, which permits any non-commercial use, sharing, distribution and reproduction in any medium or format, as long as you give appropriate credit to the original author(s) and the source, provide a link to the Creative Commons licence, and indicate if you modified the licensed material. You do not have permission under this licence to share adapted material derived from this article or parts of it. The images or other third party material in this article are included in the article's Creative Commons licence, unless indicated otherwise in a credit line to the material. If material is not included in the article's Creative Commons licence and your intended use is not permitted by statutory regulation or exceeds the permitted use, you will need to obtain permission directly from the copyright holder. To view a copy of this licence, visit http://creativecommons.org/licenses/by-nc-nd/4.0/.

© The Author(s) 2025